

Commensurate and spiral magnetic order in the doped two-dimensional Hubbard model: Dynamical mean-field theory analysis

I. A. Goremykin¹ and A. A. Katanin^{1,2}¹*Center for Photonics and 2D Materials, Moscow Institute of Physics and Technology, Institutsky Lane 9, Dolgoprudny 141700, Moscow Region, Russia*²*M. N. Mikheev Institute of Metal Physics, Kovalevskaya Street 18, Ekaterinburg 620219, Russia*

(Received 10 January 2023; revised 11 May 2023; accepted 22 May 2023; published 5 June 2023)

We develop a dynamical mean-field theory approach for the spiral magnetic order, changing to a local coordinate frame with preferable spin alignment along the z axis, which can be considered with the impurity solvers treating the spin diagonal local Green's function. We furthermore solve the Bethe-Salpeter equations for nonuniform dynamic magnetic susceptibilities in the local coordinate frame. We apply this approach to describe the evolution of magnetic order with doping in the t - t' Hubbard model with $t' = 0.15$, which is appropriate for the description of the doped La_2CuO_4 high-temperature superconductor. We find that with doping the antiferromagnetic order changes to the (Q, π) incommensurate one and then to the paramagnetic phase. The spectral weight at the Fermi level is suppressed near half filling and continuously increases with doping. The dispersion of holes in the antiferromagnetic phase shows qualitative agreement with the results of the t - J model consideration. In the incommensurate phase we find two branches of hole dispersions, one of which crosses the Fermi level. The resulting Fermi surface forms hole pockets. We also consider the dispersion of the magnetic excitations, obtained from the nonlocal dynamic magnetic susceptibilities. The transverse spin excitations are gapless, fulfilling the Goldstone theorem; in contrast to the mean-field approach the obtained magnetic state is found to be stable. The longitudinal excitations are characterized by a small gap, showing the rigidity of the spin excitations. For realistic hopping and interaction parameters we reproduce the experimentally measured spin-wave dispersion of La_2CuO_4 .

DOI: [10.1103/PhysRevB.107.245104](https://doi.org/10.1103/PhysRevB.107.245104)

I. INTRODUCTION

The properties of a two-dimensional antiferromagnet doped by holes became one of the central interests in condensed-matter physics starting in the high- T_c era. Despite the fact that the commensurate long-range magnetic order is quickly destroyed by doping (see, e.g., Refs. [1,2]), the short-range magnetic order is present in high- T_c compounds. The observed short-range magnetic order is incommensurate with the preferred wave vector $\mathbf{Q} = (\pi, \pi - \delta)$ and small incommensurability parameter δ [1–5]. This short-range order is considered to be one of the viable scenarios for pseudogap formation [6–14]. The incommensurate magnetic order is also observed on frustrated lattices, such as the triangular lattice [15,16].

Although the long-range magnetic order is absent at substantial doping in high- T_c compounds, studying the properties of long-range commensurate and incommensurate magnetic ordered states in the two-dimensional Hubbard model represents a certain interest since such order models properties of the paramagnetic phase with pronounced magnetic correlations. As a result, mean-field studies were performed to investigate the commensurate [17,18] and incommensurate spiral [19–25] magnetic orders in the doped square lattice Hubbard model. Incommensurate magnetic order on the same lattice was later studied within the slave-boson approach in Ref. [26]. The latter studies [22–24,26] showed, however,

that the incommensurate magnetically ordered states in the hole-doped Hubbard model are thermodynamically unstable within the mean-field approach, which yields a phase separation [24,26] of incommensurate magnetic order into domains with incommensurate and commensurate magnetic states. However, the above-discussed mean-field approaches do not consider (or consider only approximately for the slave-boson approach) the effect of local electronic correlations, which are important for sufficiently strong Coulomb repulsion.

The dynamical mean-field theory (DMFT) approach offers the possibility of studying commensurate [27] and incommensurate spiral [28,29] magnetic orders while taking into account local magnetic correlations. While the commensurate magnetic order within the DMFT approach for the square lattice Hubbard model is also shown to suffer from phase separation [30], a detailed analysis of the possibility of incommensurate magnetic order in the doped Hubbard model on the square lattice was not performed, to our knowledge, except for the case of only nearest-neighbor hopping [28]. Moreover, to analyze the stability of incommensurate magnetic order, nonlocal dynamic magnetic susceptibilities should be considered. While a general formalism for calculating such susceptibilities was recently proposed [31], its application to the incommensurate magnetically ordered phase is challenging.

In the present paper we reformulate the dynamical mean-field theory approach for the treatment of an incommensurate spiral magnetic order in the Hubbard model in a way that

allows using impurity solvers which treat spin diagonal local Green's functions. We furthermore apply the formalism of Ref. [31] to treat nonlocal magnetic static and dynamic susceptibilities. We consider the square lattice Hubbard model with nearest- and next-nearest-neighbor hopping and calculate the sublattice magnetization and incommensurability parameter as a function of doping and obtain longitudinal and transverse magnetic excitation spectra.

The plan of the paper is as follows. In Sec. II we formulate the model and present the method to treat commensurate and incommensurate ordered states. In Sec. III we present the results for the Fermi surfaces, the hole dispersion, and the dispersion of longitudinal and transverse magnetic excitations, obtained from the dynamic spin susceptibility. In Sec. IV we present our conclusions. In the Appendix we discuss the relation of the considered approach to the static mean-field theory.

II. MODEL AND METHOD

We consider the Hubbard model on the square lattice

$$H = - \sum_{i,j,\sigma} t_{ij} c_{i\sigma}^\dagger c_{j\sigma} + U \sum_i n_{i\uparrow} n_{i\downarrow}, \quad (1)$$

with hopping $t_{ij} = t$ between nearest neighbors (which is used as a unit of energy) and $t_{ij} = -t'$ for next-nearest neighbors. We consider spiral spin density wave magnetic order with wave vector \mathbf{Q} , which is, in general, incommensurate.

A. Derivation of DMFT equations in the spiral case

To study the model (1) we apply the DMFT approach [27]. For the commensurate case $\mathbf{Q} = (\pi, \pi)$ the DMFT equations are standard (see Ref. [27]). To study incommensurate spiral order we perform rotation of the coordinate system in spin space by an angle $\theta = \mathbf{Q}\mathbf{r}_i$ to the local coordination frame, in which the preferred direction of the spin alignment is along the z direction. This is different from the approach of Refs. [28,29], where the spins were aligned along the x direction. The advantage of having the spin alignment along the z direction lies in its codirection with the spin-quantization axes. In this case the electron Green's functions become spin diagonal in the local coordinate frame. This allows us to use the segment version of the continuous-time quantum Monte Carlo (CT-QMC) solver to treat density-density interactions (see below).

Let us consider a spiral spin density wave with spins rotating in the xz plane with wave vector \mathbf{Q} . We consider operators $d_{i\sigma}$ and $d_{i\sigma}^+$ in a local coordinate system where all spins are aligned along the z axis. To this end we perform the unitary transformation

$$\begin{pmatrix} d_{i\uparrow} \\ d_{i\downarrow} \end{pmatrix} = \begin{pmatrix} \cos(\theta/2) & \sin(\theta/2) \\ -\sin(\theta/2) & \cos(\theta/2) \end{pmatrix} \begin{pmatrix} c_{i\uparrow} \\ c_{i\downarrow} \end{pmatrix}. \quad (2)$$

The on-site Hubbard interaction is $SU(2)$ invariant,

$$n_{i\uparrow} n_{i\downarrow} = d_{i\uparrow}^+ d_{i\uparrow} d_{i\downarrow}^+ d_{i\downarrow}.$$

Therefore, the local problem is formulated straightforwardly,

$$\begin{aligned} S_{\text{loc}} = & -T \sum_{\sigma} \int_0^{\beta} d\tau \int_0^{\beta} d\tau' \zeta_{\sigma}^{-1}(\tau - \tau') d_{i\sigma}^+ d_{i\sigma} \\ & + U \int_0^{\beta} d\tau d_{i\uparrow}^+ d_{i\uparrow} d_{i\downarrow}^+ d_{i\downarrow}, \end{aligned} \quad (3)$$

where $\zeta_{\sigma}(\tau - \tau')$ is the bath Green's function.

Let us now consider the nonlocal part. We consider Fourier transformed operators

$$c_{\mathbf{k}\sigma} = \sum_{\sigma'} (\mathcal{M}_{\sigma\sigma'}^+ d_{\mathbf{k}+\mathbf{Q}/2,\sigma'} + \mathcal{M}_{\sigma\sigma'}^- d_{\mathbf{k}-\mathbf{Q}/2,\sigma'})/2, \quad (4)$$

where

$$\mathcal{M}^{\pm} = \begin{pmatrix} 1 & \pm i \\ \mp i & 1 \end{pmatrix} = \sigma^0 \mp \sigma^y \quad (5)$$

and σ^a are the Pauli matrices. Therefore,

$$\begin{aligned} c_{\mathbf{k}\uparrow}^+ c_{\mathbf{k}\uparrow} + c_{\mathbf{k}\downarrow}^+ c_{\mathbf{k}\downarrow} &= \sum_{\alpha,\sigma\sigma'} (d_{\mathbf{k}+\alpha\mathbf{Q}/2,\sigma}^+ \mathcal{M}_{\sigma\sigma'}^{\alpha} d_{\mathbf{k}+\alpha\mathbf{Q}/2,\sigma'})/2 \\ &= \sum_{\alpha} D_{\mathbf{k}+\alpha\mathbf{Q}/2,\alpha}^+ D_{\mathbf{k}+\alpha\mathbf{Q}/2,\alpha}, \end{aligned} \quad (6)$$

where $\alpha = \pm 1$ is the band index and we have introduced the operators

$$D_{\mathbf{k},\pm} = (d_{\mathbf{k}\uparrow} \pm i d_{\mathbf{k}\downarrow})/\sqrt{2}. \quad (7)$$

The kinetic term then reads

$$\sum_{\mathbf{k}\sigma} \epsilon_{\mathbf{k}} c_{\mathbf{k}\sigma}^+ c_{\mathbf{k}\sigma} = \sum_{\mathbf{k}\alpha} \epsilon_{\mathbf{k}-\alpha\mathbf{Q}/2} D_{\mathbf{k}\alpha}^+ D_{\mathbf{k}\alpha}, \quad (8)$$

where $\epsilon_{\mathbf{k}} = -2t(\cos k_x + \cos k_y) + 4t' \cos k_x \cos k_y$. Denoting the self-energy in the rotated frame $d_{i\sigma}^+$ and $d_{i\sigma}$ as $\Sigma_{\sigma}(i\nu)$, we write the lattice Green's function in the form

$$G_{\mathbf{k}}^{\sigma\sigma'}(i\nu) = -\langle d_{\mathbf{k}\sigma}(\tau) d_{\mathbf{k}\sigma'}^+(0) \rangle_{i\nu} = \left(\begin{array}{cc} i\nu + \mu - \Sigma_{\uparrow} - \frac{\epsilon_{\mathbf{k}-\mathbf{Q}/2} + \epsilon_{\mathbf{k}+\mathbf{Q}/2}}{2} & \frac{\epsilon_{\mathbf{k}-\mathbf{Q}/2} - \epsilon_{\mathbf{k}+\mathbf{Q}/2}}{2i} \\ -\frac{\epsilon_{\mathbf{k}-\mathbf{Q}/2} - \epsilon_{\mathbf{k}+\mathbf{Q}/2}}{2i} & i\nu + \mu - \Sigma_{\downarrow} - \frac{\epsilon_{\mathbf{k}-\mathbf{Q}/2} + \epsilon_{\mathbf{k}+\mathbf{Q}/2}}{2} \end{array} \right)^{-1}. \quad (9)$$

In the explicit form

$$G_{\mathbf{k}}^{\sigma\sigma}(i\nu) = \frac{i\nu + \mu - (\epsilon_{\mathbf{k}-\mathbf{Q}/2} + \epsilon_{\mathbf{k}+\mathbf{Q}/2})/2 - \Sigma_{-\sigma}(i\nu)}{(\phi_{\nu} - \epsilon_{\mathbf{k}-\mathbf{Q}/2})(\phi_{\nu} - \epsilon_{\mathbf{k}+\mathbf{Q}/2}) - [\Sigma_{\uparrow}(i\nu) - \Sigma_{\downarrow}(i\nu)]^2/4}, \quad (10)$$

$$G_{\mathbf{k}}^{\sigma,-\sigma}(i\nu) = \frac{i\sigma(\epsilon_{\mathbf{k}-\mathbf{Q}/2} - \epsilon_{\mathbf{k}+\mathbf{Q}/2})/2}{(\phi_{\nu} - \epsilon_{\mathbf{k}-\mathbf{Q}/2})(\phi_{\nu} - \epsilon_{\mathbf{k}+\mathbf{Q}/2}) - [\Sigma_{\uparrow}(i\nu) - \Sigma_{\downarrow}(i\nu)]^2/4}, \quad (11)$$

where $\phi_{\nu} = i\nu + \mu - [\Sigma_{\uparrow}(i\nu) + \Sigma_{\downarrow}(i\nu)]/2$.

The self-consistent equation reads

$$G_{\text{loc}}^{\sigma}(i\nu) \equiv \frac{1}{\zeta_{\sigma}^{-1}(i\nu) - \Sigma_{\sigma}(i\nu)} = \sum_{\mathbf{k}} G_{\mathbf{k}}^{\sigma\sigma}(i\nu). \quad (12)$$

As we discuss in the Appendix, in the mean-field approximation for the Anderson impurity model $\Sigma_{\sigma} = Un_{-\sigma}$, Eq. (12) allows us to reproduce the standard mean-field approach for the incommensurate spin density wave order. Note also that for the commensurate case the Green's functions $G_{\mathbf{k}}^{\sigma\sigma}(i\nu)$ and $G_{\mathbf{k}}^{\sigma,-\sigma}(i\nu)$ correspond to the intra- and intersublattice Green's functions in the approaches, which split the lattice into two sublattices. This establishes the relation between the DMFT approaches for the commensurate and incommensurate cases.

The corresponding lattice Green's functions for $\mathbf{Q} \neq \mathbf{0}$ read

$$\begin{aligned} \mathfrak{G}_{\mathbf{k}\sigma}(i\nu) &= -\langle T c_{\mathbf{k}\sigma}(\tau) c_{\mathbf{k}\sigma}^{\dagger}(0) \rangle_{i\nu} \\ &= \frac{1}{4} \sum_{\sigma', \alpha = \pm 1} [G_{\mathbf{k}+\alpha\mathbf{Q}/2}^{\sigma'\sigma'}(i\nu) - i\alpha\sigma' G_{\mathbf{k}+\alpha\mathbf{Q}/2}^{\sigma',-\sigma'}(i\nu)]. \end{aligned} \quad (13)$$

Note that the resulting Green's function does not depend on spin projection.

B. Relation of the two-particle quantities in the global and local reference frames

For the two-particle quantities of c operators we find the following representation in terms of d operators:

$$\sum_{\mathbf{k}} c_{\mathbf{k}}^{\dagger} \sigma^{0,y} c_{\mathbf{k}+\mathbf{q}} = \sum_{\mathbf{k}} d_{\mathbf{k}}^{\dagger} \sigma^{0,y} d_{\mathbf{k}+\mathbf{q}}, \quad (14)$$

$$\sum_{\mathbf{k}} c_{\mathbf{k}}^{\dagger} \sigma^{\pm} c_{\mathbf{k}+\mathbf{q}} = \sum_{\mathbf{k}} d_{\mathbf{k}}^{\dagger} \sigma^{\pm} d_{\mathbf{k}\pm\mathbf{Q}+\mathbf{q}}, \quad (15)$$

where $\sigma^{\pm} = \sigma^z \pm i\sigma^x$ are the in-plane spin raising and lowering matrices.

For the out-of-plane spin component y and the density correlators we therefore have

$$\begin{aligned} &\sum_{\mathbf{k}, \mathbf{k}'} \langle \langle c_{\mathbf{k}}^{\dagger} \sigma^{0,y} c_{\mathbf{k}+\mathbf{q}} | c_{\mathbf{k}'}^{\dagger} \sigma^{0,y} c_{\mathbf{k}'-\mathbf{q}} \rangle \rangle \\ &= \sum_{\mathbf{k}, \mathbf{k}'} \langle \langle d_{\mathbf{k}}^{\dagger} \sigma^{0,y} d_{\mathbf{k}+\mathbf{q}} | d_{\mathbf{k}'}^{\dagger} \sigma^{0,y} d_{\mathbf{k}'-\mathbf{q}} \rangle \rangle, \end{aligned} \quad (16)$$

while for the in-plane spin components we have

$$\begin{aligned} &\sum_{\mathbf{k}, \mathbf{k}'} \langle \langle c_{\mathbf{k}}^{\dagger} \sigma^a c_{\mathbf{k}+\mathbf{q}} | c_{\mathbf{k}'}^{\dagger} \sigma^b c_{\mathbf{k}'-\mathbf{q}} \rangle \rangle \\ &= \sum_{\mathbf{k}, \mathbf{k}'} \langle \langle d_{\mathbf{k}}^{\dagger} \sigma^a d_{\mathbf{k}+\mathbf{q}} | d_{\mathbf{k}'}^{\dagger} \sigma^b d_{\mathbf{k}'-\mathbf{q}} \rangle \rangle \delta_{\mathbf{q}+\mathbf{a}\mathbf{Q}, \mathbf{q}'-\mathbf{b}\mathbf{Q}}, \end{aligned} \quad (17)$$

where $a, b = \pm$. We note that the in-plane and out-of-plane (or density) excitations are generally coupled in the local coordinate frame (see the next section), which also yields coupling of these excitations in the global coordinate frame via the nonzero correlators $\langle \langle c_{\mathbf{k}}^{\dagger} \sigma^{0,y} c_{\mathbf{k}+\mathbf{q}} | c_{\mathbf{k}'}^{\dagger} \sigma^{\pm} c_{\mathbf{k}'-\mathbf{q}} \rangle \rangle$ at $\mathbf{q}' = \mathbf{q} \pm \mathbf{Q}$ (cf. Ref. [22]). At the same time, the correlators in the local coordinate frame are diagonal in momentum, which makes this frame somewhat more advantageous than the standard global coordinate frame considered in Ref. [22].

In the commensurate case ($2\mathbf{Q} \equiv 0$) we find

$$\begin{aligned} &\sum_{\mathbf{k}, \mathbf{k}'} \langle \langle c_{\mathbf{k}}^{\dagger} \sigma^{x,z} c_{\mathbf{k}+\mathbf{q}} | c_{\mathbf{k}'}^{\dagger} \sigma^{x,z} c_{\mathbf{k}'-\mathbf{q}} \rangle \rangle \\ &= \sum_{\mathbf{k}, \mathbf{k}'} \langle \langle d_{\mathbf{k}}^{\dagger} \sigma^{x,z} d_{\mathbf{k}+\mathbf{q}} | d_{\mathbf{k}'}^{\dagger} \sigma^{x,z} d_{\mathbf{k}'-\mathbf{q}} \rangle \rangle, \end{aligned} \quad (18)$$

which corresponds to the decoupling of longitudinal and transverse in-plane excitations in this case (see also the next section).

C. Calculation of the nonlocal susceptibilities in the local reference frame

To study the two-particle properties we perform ladder summation of the diagrams for the nonuniform dynamic susceptibility in the particle-hole channel (cf. Refs. [32–34])

$$\begin{aligned} \chi_q^{\text{mm}'} &= \sum_{k, k'} \langle \langle d_{k,\sigma}^{\dagger} d_{k+q,\sigma'} | d_{k'+q,\sigma''}^{\dagger} d_{k',\sigma'''} \rangle \rangle \\ &= \sum_{v, v'} [(\chi_{q,v}^{0,\text{mm}'})_{\text{mm}'}^{-1} \delta_{vv'} - \Phi_{\omega, vv'}^{\text{mm}'}]_{\mu\mu'}^{-1}, \end{aligned} \quad (19)$$

where we introduce composite indexes $q = (\mathbf{q}, i\omega)$, $\mu = (v, m)$, $\mu' = (v', m')$, $m = (\sigma, \sigma')$, and $m' = (\sigma'', \sigma''')$. This ladder summation is similar to that considered previously for the paramagnetic [27,32–35] and ferro- and antiferromagnetic [31] phases and allows us to obtain the nonuniform dynamic susceptibilities within the DMFT approach, which respects conservation laws (see, e.g., Refs. [32,35,36]). The bare susceptibility is

$$\chi_{q,v}^{0,(\sigma\sigma'),(\sigma''\sigma''')} = -T \sum_{\mathbf{k}} G_{\mathbf{k}}^{\sigma''\sigma} G_{\mathbf{k}+\mathbf{q}}^{\sigma'\sigma'''}, \quad (20)$$

where we use the three-vector notations $k = (\mathbf{k}, i\nu)$ in the nonlocal Green's function $G_k^{\sigma\sigma'} = G_{\mathbf{k}}^{\sigma\sigma'}(i\nu)$ [see Eqs. (9)–(11)]. Quantities with composite spin indexes m and m' can be viewed as 4×4 matrices with the indexes labeled in the order $\uparrow\uparrow, \uparrow\downarrow, \downarrow\uparrow, \text{ and } \downarrow\downarrow$. The matrix-valued local irreducible vertex $\hat{\Phi}$ then takes the form

$$\hat{\Phi}_{\omega, vv'} = \begin{pmatrix} \Phi_{\omega, vv'}^{\parallel, \uparrow\uparrow} & 0 & 0 & \Phi_{\omega, vv'}^{\parallel, \uparrow\downarrow} \\ 0 & \Phi_{\omega, vv'}^{\perp, \uparrow\downarrow} & 0 & 0 \\ 0 & 0 & \Phi_{\omega, vv'}^{\perp, \downarrow\uparrow} & 0 \\ \Phi_{\omega, vv'}^{\parallel, \downarrow\uparrow} & 0 & 0 & \Phi_{\omega, vv'}^{\parallel, \downarrow\downarrow} \end{pmatrix}, \quad (21)$$

where the components $\Phi^{\parallel, \perp}$ in longitudinal and transverse channels are evaluated from local vertices $\Gamma^{\parallel, \perp}$ in the corresponding channel via the Bethe-Salpeter equations

$$\Gamma_{\omega, vv'}^{\parallel, \sigma\sigma'} = [(\Phi_{\omega, vv'}^{\parallel, \sigma\sigma'})_{\lambda\lambda'}^{-1} - \chi_{\omega, v}^{0, \parallel, \sigma\sigma'} \delta_{vv'}]_{\lambda\lambda'}^{-1}, \quad (22)$$

$$\Gamma_{\omega, vv'}^{\perp, \sigma, -\sigma} = [(\Phi_{\omega, vv'}^{\perp, \sigma, -\sigma})^{-1} - \chi_{\omega, v}^{0, \perp, \sigma, -\sigma} \delta_{vv'}]_{vv'}^{-1}, \quad (23)$$

where composite indexes $\lambda = (\sigma, v)$ and $\lambda' = (\sigma', v')$, local bare susceptibilities are $\chi_{\omega, v}^{0, \parallel, \sigma\sigma'} = -T G_{\text{loc}}^{\sigma}(i\nu) G_{\text{loc}}^{\sigma'}(i\nu + i\omega) \delta_{\sigma\sigma'}$ and $\chi_{\omega, v}^{0, \perp, \sigma\sigma'} = -T G_{\text{loc}}^{\sigma}(i\nu) G_{\text{loc}}^{\sigma'}(i\nu + i\omega)$. Finally, the local vertices $\Gamma_{\omega, vv'}^{\parallel(\perp), \sigma\sigma'}$ for both channels are obtained from the single-impurity problem.

Further, performing the same steps as in Refs. [33,34], we find the irreducible susceptibility ϕ_q fulfilling the matrix relation

$$\hat{\chi}_q = (\hat{I} - \hat{\phi}_q \hat{U})^{-1} \hat{\phi}_q \quad (24)$$

in the form

$$\hat{\phi}_q = \hat{\chi}_q^0 \hat{\gamma}_q + \hat{X}_q, \quad (25)$$

where $\hat{X}_q^{\text{mm}'} = \sum_{\nu \notin B} \chi_{q,\nu}^{0,\text{mm}'}$ accounts for the contribution of frequencies beyond the considered frequency box B ,

$$\hat{U} = \begin{pmatrix} 0 & 0 & 0 & -U \\ 0 & U & 0 & 0 \\ 0 & 0 & U & 0 \\ -U & 0 & 0 & 0 \end{pmatrix}, \quad (26)$$

and \hat{I} is the 4×4 identity matrix. The triangular vertex has the form

$$\gamma_q^{\mu\text{m}'} = \sum_{\nu' \in B} [\hat{I} \delta_{\nu\nu'} - (\hat{\Phi}_{\omega,\nu\nu'} - \tilde{U}) \chi_{q,\nu}^{0,\mu\mu'}]^{-1}, \quad (27)$$

where $\tilde{U} = (\hat{I} - \hat{U} \hat{X}_q)^{-1} \hat{U}$. Equations (25) and (27) are used in numerical calculations of the irreducible susceptibility ϕ_q .

In the case of the wave vector $\mathbf{Q} = (\pi - \delta, \pi)$ it can be shown from the representation of the nonlocal Green's function (9) that full susceptibility satisfies the symmetry relations

$$\chi_{-q_x, q_y, \omega}^{\text{mn}} = \eta_m \eta_n \chi_{q_x, q_y, \omega}^{\text{mn}}, \quad (28)$$

$$\chi_{q_x, -q_y, \omega}^{\text{mn}} = \chi_{q_x, q_y, \omega}^{\text{mn}}, \quad (29)$$

where $\eta_{\uparrow\uparrow} = \eta_{\downarrow\downarrow} = 1$ and $\eta_{\uparrow\downarrow} = \eta_{\downarrow\uparrow} = -1$. In the commensurate case $\mathbf{Q} = (\pi, \pi)$, in addition to symmetry relations (28) and (29), $\hat{\chi}_q$ satisfies

$$\chi_{-q_x, q_y, \omega}^{\text{mn}} = \chi_{q_x, q_y, \omega}^{\text{mn}}. \quad (30)$$

From the symmetry relations (28) and (30) it immediately follows that in the commensurate case $\mathbf{Q} = (\pi, \pi)$ the longitudinal and transverse channels are decoupled from each other:

$$\chi^{\sigma\sigma\sigma, -\sigma} = \chi^{\sigma\sigma, -\sigma\sigma} = \chi^{\sigma, -\sigma\sigma\sigma} = \chi^{-\sigma, \sigma\sigma\sigma} = 0. \quad (31)$$

This decoupling was also noted in Refs. [18,31].

To solve the DMFT impurity problem and calculate local vertices we have used the CT-QMC impurity solver, implemented in the iQIST software package [37]. To obtain static and dynamic properties we had to complete an analytical continuation of our results from the imaginary frequency axis to the real frequency axis. For this purpose we used the ANA_CONT PYTHON package [38].

III. RESULTS

We consider $t' = 0.15t$, which is a typical value for $\text{La}_{2-x}\text{Sr}_x\text{CuO}_4$, and set the temperature $T = 0.1t$. We calculate the susceptibilities $\chi^{ab}(\mathbf{q}, \omega) \equiv \sum_{\text{mm}'} \sigma_m^a \chi_q^{\text{mm}'} \sigma_m^b$, where $a, b = x, y, z$. The initial wave vector \mathbf{Q} is obtained by providing the minimum of the minimal eigenvalue of the matrix $\hat{I} - \hat{\phi}_q \hat{U}$ at $\omega = 0$ in the antiferromagnetic phase and then determined self-consistently to provide the minimum of the

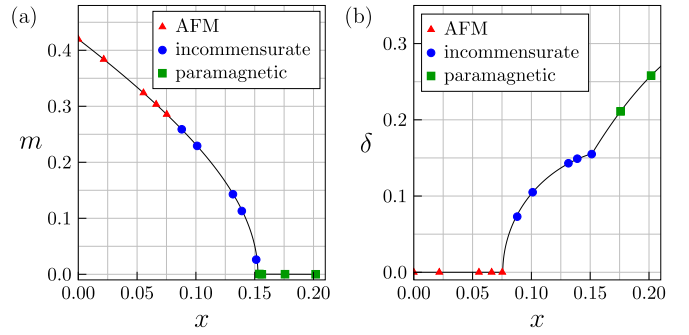


FIG. 1. Dependence of (a) staggered magnetization $m = \langle S_Q^- \rangle$ and (b) the incommensurability parameter δ of the magnetic order on the hole doping level x at $U/t = 7.5$. Triangles denote the antiferromagnetic state, circles indicate states with incommensurate magnetic order, and squares represent the paramagnetic state.

minimal eigenvalue of the same matrix in the incommensurate case.

In all calculations we find that the dominant wave vector $\mathbf{Q} = (\pi - \delta, \pi)$, in agreement with earlier slave-boson studies [26] and similar to the wave vector of short-range magnetic order observed in $\text{La}_{2-x}\text{Sr}_x\text{CuO}_4$ [1–5]. We note that the mean-field approach [22,24] yields the dominating phase $\mathbf{Q} = (Q, Q)$ at a sufficiently strong interaction U of the order of the bandwidth, which seems to be the drawback of neglecting correlations in this approach.

In Fig. 1(a) we plot the dependence of staggered magnetization $m = \langle S_Q^- \rangle$, where $\hat{S}^\pm = \hat{S}^z \pm i\hat{S}^x$, on the hole doping $x = 1 - n$ at $U/t = 7.5$. Staggered magnetization shows mean-field-like behavior $m \propto \sqrt{x_c - x}$ near the critical value of hole doping level $x_c \approx 0.15$. Although the sublattice magnetization is continuous with doping, there are two different types of states with $x < x_c$. At low doping ($x < x_c^{(Q)}$) we find antiferromagnetic magnetic order [marked by triangles in Fig. 1(a)]. At intermediate values of the hole doping level we obtain incommensurate magnetic order: the spin density wave [circles in Fig. 1(a)]. The dependence of the degree of incommensurability δ of the magnetic order on the doping level x is presented in Fig. 1(b). Close to the commensurate-incommensurate transition this dependence is quite similar to the one observed for the short-range magnetic order in $\text{La}_{2-x}\text{Sr}_x\text{CuO}_4$ [39,40].

Using analytical continuation of the self-energy $\Sigma_\sigma(\nu)$, which takes into account the constant and $1/\nu$ asymptotics of the self-energy at large frequencies [38,41], we obtain the electron spectral functions $A(\mathbf{k}, \nu) = -\text{Im}\mathfrak{G}_{\mathbf{k}\sigma}(\nu)/\pi$, as well as the local spectral function $A(\nu) = \sum_{\mathbf{k}} A(\mathbf{k}, \nu)$. In Fig. 2 we show $A(\nu)$ for various doping levels. The quasiparticle peak is shifted below the Fermi level and corresponds to the hole states in the antiferromagnetic or spiral spin density wave background. At very low doping we find the gap in the spectrum at the Fermi level, which is present because of the redistribution of the spectral weight between the Hubbard (Slater) subbands, as well as thermal activation of the electron-hole pairs (see more details in the Appendix). The gap is continuously filled with a further increase of the doping. Continuous increase of the spectral weight at the

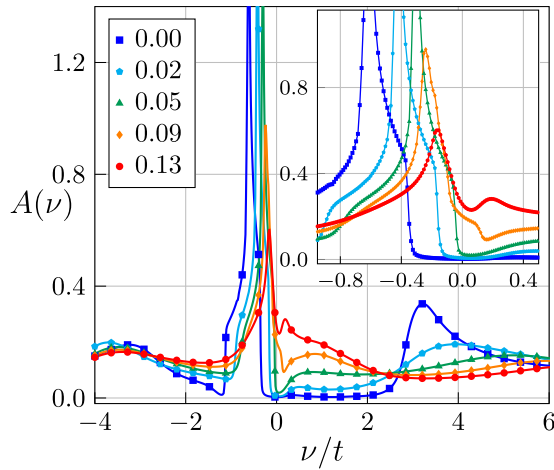


FIG. 2. Electron local spectral functions $A(\nu)$ at $U/t = 7.5$ for various values of doping level x indicated in the legend. The inset shows the low-energy region, containing quasiparticle peaks and the spectral gaps.

Fermi level with doping agrees with the experimental data for $\text{La}_{2-x}\text{Sr}_x\text{CuO}_4$ [42].

In Fig. 3 we show the contour plots of the zero energy $A(\mathbf{k}, \nu = 0)$ spectral functions, whose maxima show the positions of the Fermi surfaces. At small hole doping the Fermi pockets are absent since the Fermi level lies in the gap of the spectral function. In the incommensurate state [see Fig. 3(a) for hole doping level $x = 0.11$] the Fermi surface consists of hole pockets. It is spin independent and symmetric under each of the transformations $k_x \rightarrow -k_x$ and $k_y \rightarrow -k_y$. At the same time, the Fermi surface for the paramagnetic state [see Fig. 3(b) for hole doping level $x = 0.20$] is connected and has the standard shape.

In Fig. 4 we show the hole dispersion, obtained from the contour plots of hole spectral functions $A(\mathbf{k}, -\nu)$, for the antiferromagnetic state (doping $x = 0.05$) and the incommensurate state (doping $x = 0.11$). Hole dispersion calculated in the antiferromagnetic state qualitatively coincides with the results obtained for the t - J model (see, e.g., Refs. [43,44]).

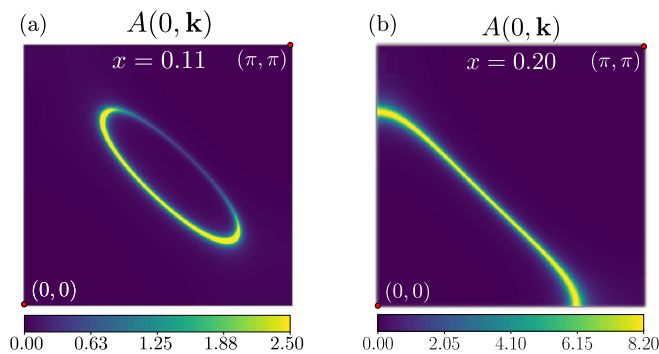


FIG. 3. The zero-energy spectral functions showing the positions of the Fermi surface in the upper right quadrant of the Brillouin zone at $U/t = 7.5$. (a) The state with incommensurate magnetic ordering at hole doping level $x = 0.11$. (b) Paramagnetic state at hole doping level $x = 0.20$.

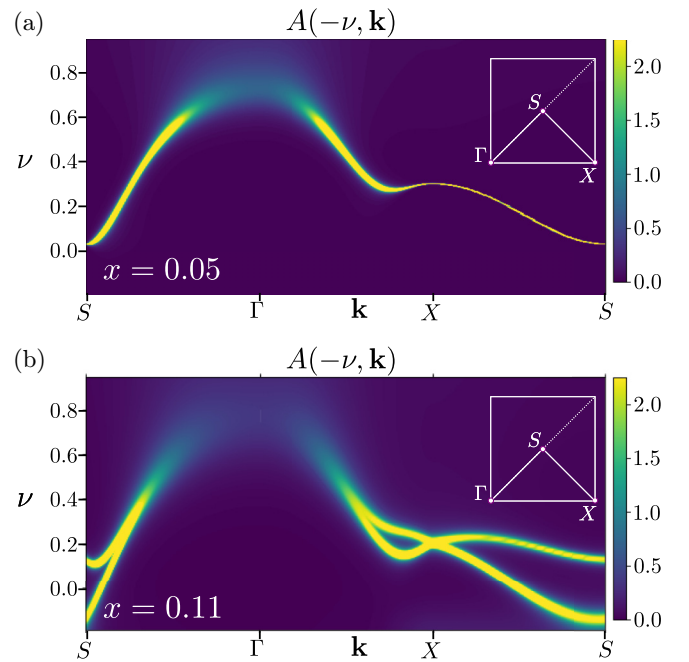


FIG. 4. The frequency and momentum dependence of the spectral functions at negative energy, showing the dispersion relation of holes at $U/t = 7.5$ in (a) the antiferromagnetic state at doping $x = 0.05$, and (b) the incommensurate state at doping $x = 0.11$. The Fermi level corresponds to zero energy. Positions of high-symmetry points in the upper right quadrant of the first Brillouin zone are shown in the inset.

However, in contrast to earlier studies, in the antiferromagnetic state it does not cross the Fermi level. Low spectral weight at the Fermi level, which is seen in Fig. 2, appears in this case from the accumulation of the tails of the peaks in the k -resolved spectral functions. At the same time, two different hole dispersion branches are present in the incommensurate case, which originate from the $\mathbf{k} \pm \mathbf{Q}/2$ contributions in Eq. (13). The lower dispersion branch in this case forms the Fermi surface pocket. When the system changes to the antiferromagnetic phase, the two modes merge. We have verified that in both commensurate and incommensurate cases the main contribution to the dispersion comes from the first term in the second line of Eq. (13) with $\sigma' = \uparrow$, i.e., the diagonal spin-majority states. The local vertex approximation and analytical continuation of bosonic quantities allow us to calculate different components of the dynamic susceptibility $\chi(\mathbf{q}, \omega) \equiv \chi_{\mathbf{q}}$. Its matrix-valued nature in our formalism provides an opportunity to investigate different types of magnetic excitations, which are coupled to each other for the incommensurate order, as was emphasized in Ref. [22].

In Fig. 5 we show the corresponding susceptibilities in the doped commensurate case for $x = 0.05$. As discussed in Sec. II B, in the state with the commensurate antiferromagnetic order the “longitudinal” excitations, determined by the maximum of the susceptibility $\text{Im}[\chi^{zz}(\mathbf{q}, \omega)]$, are decoupled from the transverse ones, determined by $\text{Im}[\chi^{xx,yy}(\mathbf{q}, \omega)]$. From the $\chi^{xx,yy}(\mathbf{q}, \omega)$ susceptibilities we obtain massless Goldstone modes, which are related to the spontaneous symmetry breaking. Their spectrum broadens rapidly with the

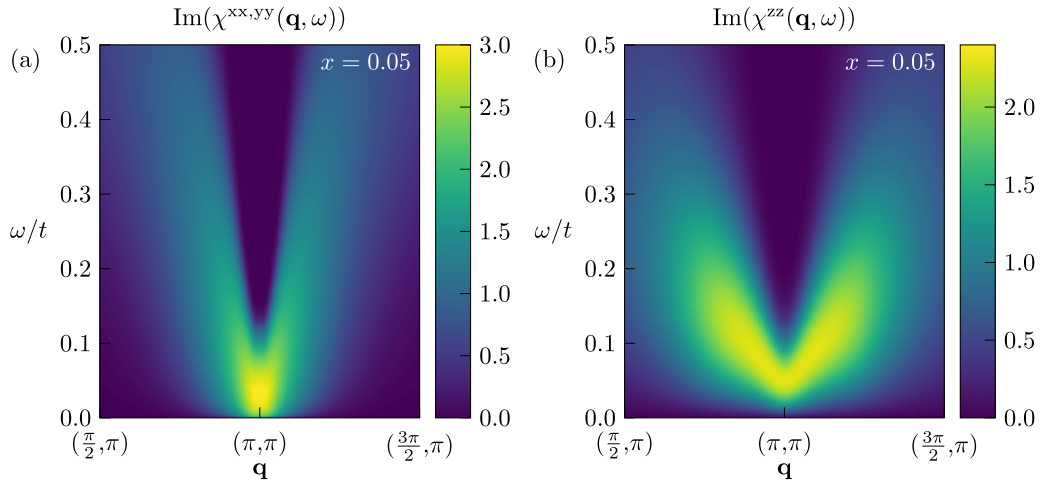


FIG. 5. Imaginary part of (a) the transverse $\chi^{xx,yy}$ (logarithmic color scale) and (b) longitudinal χ^{zz} (linear color scale) dynamic magnetic susceptibilities as a function of the energy ω and the vector \mathbf{q} along the path $(\pi/2, \pi) \rightarrow (3\pi/2, \pi)$ for the antiferromagnetic state at hole doping $x = 0.05$ and $U/t = 7.5$.

deviation of the wave vector \mathbf{q} from $\mathbf{Q} = (\pi, \pi)$. We do not find evidence of negative modes in the magnon's spectrum. This shows that the considered $\mathbf{Q} = (\pi - \delta, \pi)$ order is stable. The longitudinal excitations, obtained from $\text{Im}\chi^{zz}(\mathbf{q}, \omega)$, possess a gap of the order of $0.1t$. Similar to the transverse channel, the longitudinal excitations become less coherent with the deviation of the wave vector \mathbf{q} from \mathbf{Q} .

In the incommensurate case the longitudinal and transverse excitations are coupled. Accordingly, we analyze the in-plane excitations, determined by $\text{Im}[\chi^{+-}(\mathbf{q}, \omega)]$ susceptibility of \hat{S}^{\pm} spin components, and the out-of-plane component, determined by $\text{Im}[\chi^{yy}(\mathbf{q}, \omega)]$. In Fig. 6 we show the corresponding susceptibilities for the incommensurate state far from transitions to paramagnetic and antiferromagnetic states. In $\text{Im}[\chi^{yy}(\mathbf{q}, \omega)]$ we find two Goldstone modes at wave vectors $\mathbf{q} = \pm\mathbf{Q}$. They merge at $\mathbf{q} = (\pi, \pi)$ when the order changes to the antiferromagnetic one. In the in-plane component $\text{Im}[\chi^{+-}(\mathbf{q}, \omega)]$ there is also a Goldstone mode at $\mathbf{q} =$

$-\mathbf{Q}$, corresponding to transverse excitations, while at $\mathbf{q} = \mathbf{Q}$ we observe a longitudinal (Higgs) mode of weaker intensity. As in the commensurate case, this mode is gapped. Upon approaching the paramagnetic phase (see Fig. 7) the longitudinal mode softens, and the corresponding gap disappears at the spin density wave to the paramagnet transition. Like in the commensurate case, no evidence of instability of the considered long-range order is obtained, such that this order appears to be stable.

We have verified that the presented results remain qualitatively unchanged for larger values of U/t , except that the incommensurate region of doping levels becomes narrower with the increase of U/t at fixed temperature T . The considered value $U/t = 7.5$ corresponds to the metallic state at half filling in the absence of long-range antiferromagnetic order, and it is also somewhat smaller than typically considered for cuprate high- T_c compounds. To compare the obtained magnon dispersions with the experimental data for cuprates, in Fig. 8

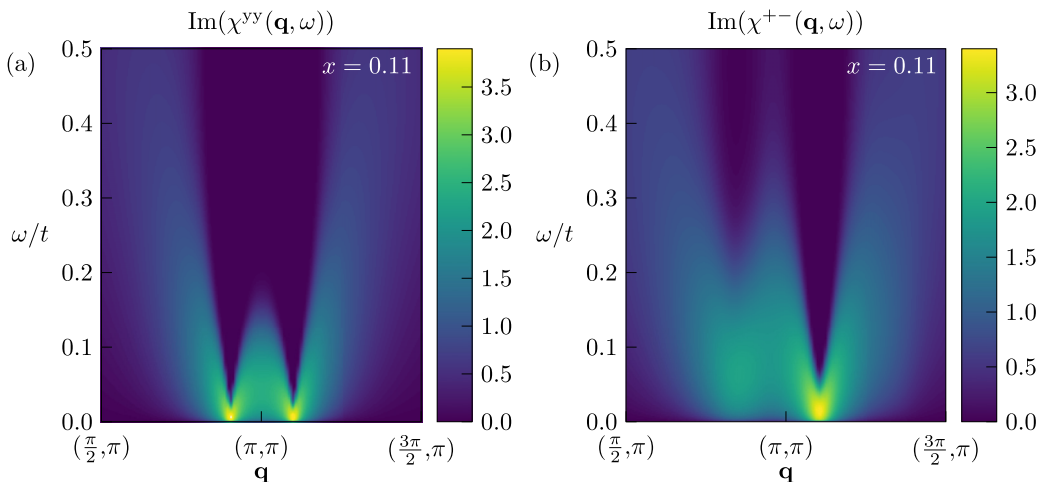


FIG. 6. Imaginary part of (a) the out-of-plane χ^{yy} and (b) the in-plane χ^{+-} dynamic magnetic susceptibilities (logarithmic color scale) as a function of the energy ω and momentum \mathbf{q} along the path $(\pi/2, \pi) \rightarrow (3\pi/2, \pi)$ for hole doping $x = 0.11$ (corresponding incommensurability $\delta = 0.10$) and $U/t = 7.5$.

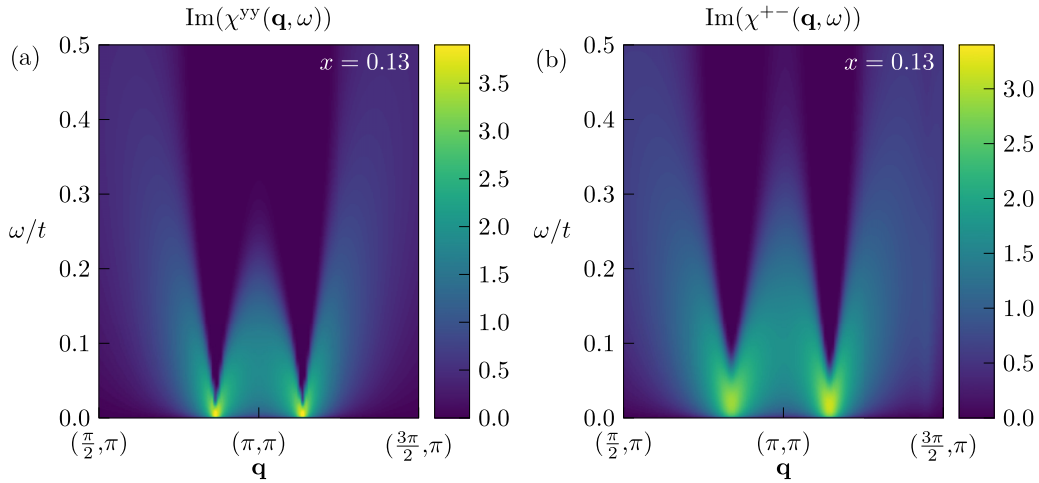


FIG. 7. The same as Fig. 6 for hole doping $x = 0.13$ (corresponding incommensurability $\delta = 0.13$).

we show the magnon dispersion for $U = 10t$. We consider an antiferromagnetic state at small doping $x = 0.01$ to avoid difficulties with analytic continuation of dynamic susceptibilities at half filling. The obtained dispersion is compared to the experimental data of Ref. [45] at half filling. We can see that for the hopping $t = 425$ meV the obtained maxima of $\text{Im}\chi^{xx,yy}(\mathbf{q}, \omega)$ compare well with the experimental dispersion, including the $(\pi, 0)$ - $(\pi/2, \pi/2)$ part, whose deviation from the flat dispersion in the linear spin-wave analysis of the Heisenberg model was previously attributed to the ring exchange (see, e.g., Refs. [45,46]). Taking into account the renormalization factor of the spin-wave dispersion of the $S = 1/2$ two-dimensional Heisenberg model [47,48] $\gamma = 1.157$, which originates from the magnon interaction and is not accounted for by the considered ladder approximation, we find the bare hopping, capable of describing the magnon dispersion $t_{\text{bare}} = t/\gamma \simeq 370$ meV, in good agreement with the estimate $J_{\text{bare}}U/(4t) \simeq t_{\text{bare}}$, considering $J_{\text{bare}} \simeq 152$ meV [46]. The maximum of the imaginary part of the longitudinal susceptibility shows longitudinal excitation with a rather small gap ~ 10 meV.

IV. CONCLUSION

In the present paper we considered the calculation of sublattice magnetization, the incommensurability parameter, hole dispersion, and the dynamic magnetic susceptibilities of the square lattice Hubbard model with nearest- and next-nearest-neighbor hopping in the antiferromagnetic and incommensurate cases within the dynamic mean-field theory. At small doping we obtained an antiferromagnetic insulating state with hole dispersion, which agrees qualitatively with that obtained previously for the t - J model. The transverse magnetic susceptibility possesses a Goldstone mode, while the longitudinal excitations are characterized by a small gap.

At larger doping we found an incommensurate spiral $\mathbf{Q} = (\pi, \pi - \delta)$ order with two branches of hole dispersions and Fermi surfaces, having the shape of hole pockets. The out-of-plane magnetic susceptibility possesses Goldstone modes at the incommensurate wave vectors, while the in-plane susceptibility shows both gapless Goldstone spin-wave excitations and the longitudinal gapped excitation. The obtained long-range order was found to be stable from the susceptibility analysis.

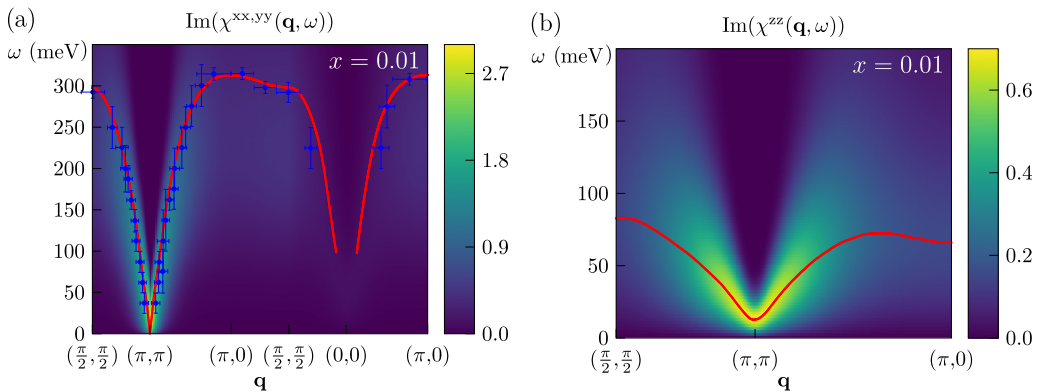


FIG. 8. Imaginary part of (a) the transverse $\chi^{xx,yy}$ (logarithmic color scale) and (b) longitudinal χ^{zz} (linear color scale) dynamic magnetic susceptibilities as a function of energy ω and the vector \mathbf{q} along symmetric directions for the commensurate antiferromagnetic state near half filling at hole doping level $x = 0.01$. The interaction $U/t = 10$, and $t = 425$ meV. The maxima of the imaginary parts are shown by the red line, except in the vicinity of the point $\mathbf{q} = 0$, where the intensity is very low and not captured by analytical continuation. The experimental data for the spin-wave dispersion at half filling, taken from Ref. [45], are represented in the left plot by blue points with error bars.

We also showed that close to half filling the experimentally observed magnon dispersion can be reproduced with reasonable values of hopping t and interaction U . The obtained doping evolution of the Fermi surfaces and the incommensurability parameter δ are quite similar to those for high- T_c cuprate superconductors, which stresses once more a possible magnetic origin of the pseudogap. Although the considered magnetic state is long range ordered, this order can be “hidden,” e.g., within the gauge theory of fluctuating spin density wave order discussed recently in Refs. [11,12,14]. The extension of the proposed approach to the paramagnetic phase within these gauge theories therefore represents a promising direction of future research. This may also concern other types of lattices, including compounds with a frustrated triangular lattice, which are candidates for the spin-liquid phase [49–52].

ACKNOWLEDGMENTS

The authors acknowledge the financial support from the BASIS Foundation (Grant No. 21-1-1-9-1) and the Ministry of Science and Higher Education of the Russian Federation (Agreement No. 075-15-2021-606). A.A.K. also acknowledges the financial support within the theme “Quant” 122021000038-7 of the Ministry of Science and Higher Education of the Russian Federation.

APPENDIX: RELATION TO THE STATIC MEAN-FIELD APPROACH

The static mean-field treatment in the considered approach is conveniently formulated by considering the (frequency-independent) mean-field approximation for the self-energy of the impurity Anderson model $\Sigma_\sigma = U n_{-\sigma}$. The corresponding occupation numbers are obtained from the equation

$$n_\sigma = T \sum_v \frac{1}{\zeta_\sigma^{-1}(iv) - U n_{-\sigma}}. \quad (\text{A1})$$

Exploiting the self-consistency equation (12), we obtain

$$T \sum_{\mathbf{k},v} G_{\mathbf{k}}^{\sigma\sigma}(iv) = n_\sigma. \quad (\text{A2})$$

Defining the mean-field order parameter

$$\Delta = \frac{\Sigma_\downarrow - \Sigma_\uparrow}{2} = Um, \quad (\text{A3})$$

where the local magnetization $m = (n_\uparrow - n_\downarrow)/2$, and taking into account the form of the Green's function (10), the summation over frequencies in Eq. (A2) can be performed analytically and yields the equation

$$\frac{1}{U} = \sum_{\mathbf{k}} \frac{f(E_v(\mathbf{k})) - f(E_c(\mathbf{k}))}{2E_-(\mathbf{k})}, \quad (\text{A4})$$

where

$$E_{c,v}(\mathbf{k}) = \epsilon_+(\mathbf{k}) \pm E_-(\mathbf{k}) - \tilde{\mu}, \quad (\text{A5})$$

$$E_-(\mathbf{k}) = \sqrt{\epsilon_-^2(\mathbf{k}) + \Delta^2}, \quad (\text{A6})$$

$$\epsilon_\pm(\mathbf{k}) = \frac{1}{2}(\epsilon_{\mathbf{k}-\mathbf{Q}/2} \pm \epsilon_{\mathbf{k}+\mathbf{Q}/2}), \quad (\text{A7})$$

$f(\varepsilon) = [\exp(\varepsilon/T) + 1]^{-1}$ is the Fermi function, and $\tilde{\mu} = \mu - (\Sigma_\uparrow + \Sigma_\downarrow)/2$. Equation (A4) allows one to determine the

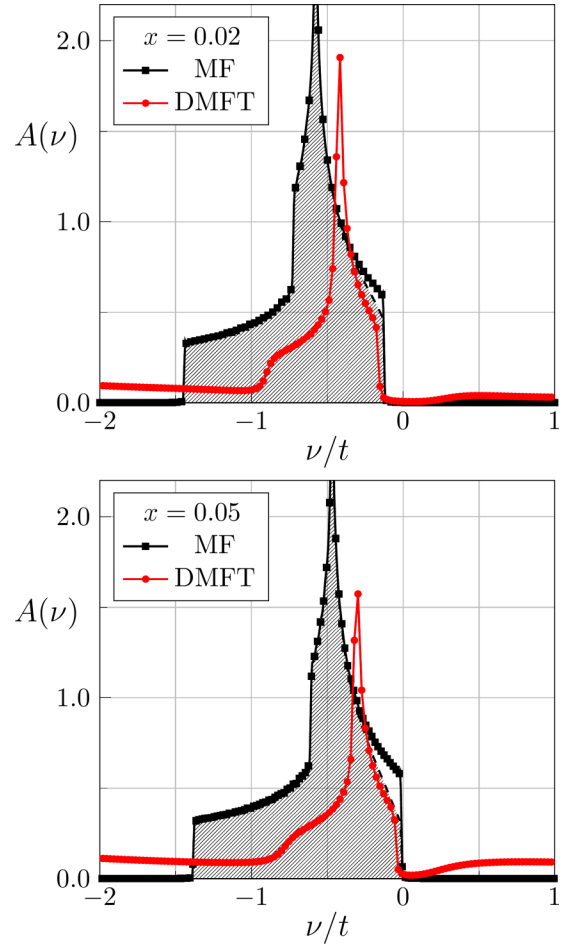


FIG. 9. Electron local spectral functions $A(\nu)$ near the Fermi level for $U/t = 7.5$, $T = 0.1t$, and hole doping levels $x = 0.02$ and $x = 0.05$ obtained using the mean-field approach (black squares). The shaded area under the dashed line, showing $A(\nu)f(\nu)$, represents partial occupancy of electronic states due to thermal smearing. The results of the DMFT approach from Fig. 2 are shown by red circles.

order parameter Δ (the chemical potential $\tilde{\mu}$ is fixed by the total number of particles) and coincides with the corresponding mean-field equation of Refs. [17–25].

Analogously, the ladder summation of diagrams for susceptibilities, considered in Refs. [17,18,20–23,25], can be reproduced for an infinite (finite) frequency box considering the bare two-particle irreducible vertices $\hat{\Phi}_{\omega,\nu\nu'} = \hat{U}(\tilde{U})$, where the matrix $\hat{U}(\tilde{U})$ is defined in Eq. (26) [after Eq. (27)]. This also implies the triangular vertex $\gamma_q^{\mu m} = \delta_{mm'}$ in the mean-field approximation.

The density of states of the lower Slater (valence) band $E_v(\mathbf{k})$ in the mean-field approach for parameter values $t' = 0.15t$, $U = 7.5t$, and $T = 0.1t$, considered in the main text, is shown in Fig. 9. For the purpose of the comparison to the DMFT approach we fix the wave vector to $\mathbf{Q} = (\pi, \pi)$. At the considered small doping and finite temperature the Fermi level lies within the spectral gap; thermal activation of holes in the valence band results in an occupancy smaller than 1, corresponding to the chosen hole doping level. This effect of thermal smearing is illustrated in Fig. 9 by the shaded area under the mean-field spectral function, which represents the

fraction of occupied states. With increasing hole doping, the Fermi level shifts closer to the valence band. This behavior of the spectral function in the mean-field approach is preserved also for small deviations of magnetic order from the Néel state.

While previous mean-field studies [22–24] showed that at the mean-field level the spiral phases are thermodynamically unstable at sufficiently strong interaction and show the regions of negative susceptibilities, as we discussed in the main text, this drawback of the mean-field theory is cured in the dynamical mean-field theory approach. As also discussed in Ref. [53], the static mean-field solution is not quantitatively correct for the symmetry-broken phases even in the limit of weak coupling. In particular, for the antiferromagnetic case, already at sufficiently small interaction, the DMFT solution differs from that of the static mean-field approach due to the development of the frequency dependence of the self-energy [54]. The same is expected for the incommensurate phases.

The spectral functions of the DMFT approach at small doping, presented in the main text (Fig. 2), show a

quasiparticle peak with the right edge only slightly shifted with respect to that of the lower Slater band of the mean-field theory, but the height of the peak remains smaller than in the mean-field theory due to partial transfer of the spectral weight to the lower Hubbard band at negative energies (see the comparison in Fig. 9). Although at finite temperatures the quasiparticle peak is also not fully filled in the DMFT even for the Fermi level position above the peak, in contrast to the mean-field approach, the spectral weight of the quasiparticle peak and lower Hubbard band [which we define as the integral weight $w = \int_{-\infty}^0 d\nu A(\nu)$] in the DMFT reduces with doping (see Figs. 2 and 9). In particular, for $x = 0.02$ and $x = 0.05$ we obtain for this weight $w = 0.99$ and $w = 0.97$, respectively [55], such that in the DMFT the spectral weight is redistributed between the lower and upper Hubbard (Slater) subbands. Therefore, in contrast to the mean-field approach, the DMFT approach, apart from the trivial thermal smearing, shows an additional many-body contribution to the spectral functions, which keeps the Fermi level inside the gap at low doping.

-
- [1] N. Plakida, *High-Temperature Cuprate Superconductors* (Springer, Heidelberg, 2010).
- [2] J. J. Wagman, G. Van Gastel, K. A. Ross, Z. Yamani, Y. Zhao, Y. Qiu, J. R. D. Copley, A. B. Kallin, E. Mazurek, J. P. Carlo, H. A. Dabkowska, and B. D. Gaulin, *Phys. Rev. B* **88**, 014412 (2013).
- [3] S.-W. Cheong, G. Aeppli, T. E. Mason, H. Mook, S. M. Hayden, P. C. Canfield, Z. Fisk, K. N. Clausen, and J. L. Martinez, *Phys. Rev. Lett.* **67**, 1791 (1991).
- [4] T. E. Mason, G. Aeppli, S. M. Hayden, A. P. Ramirez, and H. A. Mook, *Phys. Rev. Lett.* **71**, 919 (1993).
- [5] M. Matsuda, K. Yamada, Y. Endoh, T. R. Thurston, G. Shirane, R. J. Birgeneau, M. A. Kastner, I. Tanaka, and H. Kojima, *Phys. Rev. B* **49**, 6958 (1994).
- [6] J. Schmalian, D. Pines, and B. Stojkovic, *Phys. Rev. Lett.* **80**, 3839 (1998); *Phys. Rev. B* **60**, 667 (1999).
- [7] E. Z. Kuchinskii and M. V. Sadovskii, *J. Exp. Theor. Phys.* **88**, 968 (1999).
- [8] F. Onufrieva, P. Pfeuty, and M. Kiselev, *Phys. Rev. Lett.* **82**, 2370 (1999); F. Onufrieva and P. Pfeuty, *ibid.* **82**, 3136 (1999).
- [9] O. Gunnarsson, T. Schäfer, J. P. F. LeBlanc, E. Gull, J. Merino, G. Sangiovanni, G. Rohringer, and A. Toschi, *Phys. Rev. Lett.* **114**, 236402 (2015).
- [10] E. A. Stepanov, L. Peters, I. S. Krivenko, A. I. Lichtenstein, M. I. Katsnelson, and A. N. Rubtsov, *npj Quantum Mater.* **3**, 54 (2018).
- [11] W. Wu, M. S. Scheurer, S. Chatterjee, S. Sachdev, A. Georges, and M. Ferrero, *Phys. Rev. X* **8**, 021048 (2018).
- [12] M. S. Scheurer, S. Chatterjee, W. Wu, M. Ferrero, A. Georges, and S. Sachdev, *Proc. Natl. Acad. Sci. USA* **115**, E3665 (2018).
- [13] F. Krien, P. Worm, P. Chalupa-Gantner, A. Toschi, and K. Held, *Commun. Phys.* **5**, 336 (2022).
- [14] D. Vildardi, P. M. Bonetti, and W. Metzner, *Phys. Rev. B* **102**, 245128 (2020); P. M. Bonetti and W. Metzner, *ibid.* **106**, 205152 (2022).
- [15] K. Miyagawa, A. Kawamoto, Y. Nakazawa, and K. Kanoda, *Phys. Rev. Lett.* **75**, 1174 (1995).
- [16] K. Kanoda, *Phys. C (Amsterdam, Neth.)* **282–287**, 299 (1997).
- [17] J. R. Schrieffer, X. G. Wen, and S. C. Zhang, *Phys. Rev. B* **39**, 11663 (1989).
- [18] A. V. Chubukov and D. M. Frenkel, *Phys. Rev. B* **46**, 11884 (1992).
- [19] M. Dzierzawa, *Z. Phys. B* **86**, 49 (1992).
- [20] A. P. Kampf and W. Brenig, *J. Low Temp. Phys.* **95**, 335 (1994); W. Brenig, *ibid.* **99**, 319 (1995).
- [21] R. Côté and A. M. S. Tremblay, *Europhys. Lett.* **29**, 37 (1995).
- [22] A. V. Chubukov and K. A. Muehselien, *Phys. Rev. B* **51**, 12605 (1995).
- [23] A. P. Kampf, *Phys. Rev. B* **53**, 747 (1996).
- [24] P. A. Igoshev, M. A. Timirgazin, A. A. Katanin, A. K. Arzhnikov, and V. Yu. Irkhin, *Phys. Rev. B* **81**, 094407 (2010).
- [25] P. M. Bonetti and W. Metzner, *Phys. Rev. B* **105**, 134426 (2022).
- [26] P. A. Igoshev, M. A. Timirgazin, V. F. Gilmutdinov, A. K. Arzhnikov, and V. Yu. Irkhin, *J. Magn. Magn. Mater.* **383**, 2 (2015); *J. Phys.: Condens. Matter* **27**, 446002 (2015).
- [27] A. Georges, G. Kotliar, W. Krauth, and M. J. Rozenberg, *Rev. Mod. Phys.* **68**, 13 (1996).
- [28] M. Fleck, A. I. Lichtenstein, A. M. Oleś, L. Hedin, and V. I. Anisimov, *Phys. Rev. Lett.* **80**, 2393 (1998).
- [29] S. Goto, S. Kurihara, and D. Yamamoto, *Phys. Rev. B* **94**, 245145 (2016).
- [30] R. Zitzler, Th. Pruschke, and R. Bulla, *Eur. Phys. J. B* **27**, 473 (2002).
- [31] L. Del Re and A. Toschi, *Phys. Rev. B* **104**, 085120 (2021).
- [32] G. Rohringer, H. Hafermann, A. Toschi, A. A. Katanin, A. E. Antipov, M. I. Katsnelson, A. I. Lichtenstein, A. N. Rubtsov, and K. Held, *Rev. Mod. Phys.* **90**, 025003 (2018).
- [33] A. A. Katanin, *Phys. Rev. B* **101**, 035110 (2020).
- [34] A. A. Katanin, *Phys. Rev. B* **104**, 245142 (2021); **106**, 115147 (2022).
- [35] E. A. Stepanov, E. G. C. P. van Loon, A. A. Katanin, A. I. Lichtenstein, M. I. Katsnelson, and A. N. Rubtsov, *Phys. Rev. B* **93**, 045107 (2016).

- [36] F. Krien, Ph.D. thesis, Universität Hamburg, 2018.
- [37] L. Huang, Y. Wang, Z. Y. Meng, L. Du, P. Werner, and X. Dai, *Comput. Phys. Commun.* **195**, 140 (2015); L. Huang, *ibid.* **221**, 423 (2017).
- [38] J. Kaufmann and K. Held, *Comput. Phys. Commun.* **282**, 108519 (2023).
- [39] K. Yamada, C. H. Lee, K. Kurahashi, J. Wada, S. Wakimoto, S. Ueki, H. Kimura, Y. Endoh, S. Hosoya, G. Shirane, R. J. Birgeneau, M. Greven, M. A. Kastner, and Y. J. Kim, *Phys. Rev. B* **57**, 6165 (1998).
- [40] S. Wakimoto, G. Shirane, Y. Endoh, K. Hirota, S. Ueki, K. Yamada, R. J. Birgeneau, M. A. Kastner, Y. S. Lee, P. M. Gehring, and S. H. Lee, *Phys. Rev. B* **60**, 769(R) (1999).
- [41] X. Wang, H. T. Dang, and A. J. Millis, *Phys. Rev. B* **84**, 073104 (2011).
- [42] M. Hashimoto, T. Yoshida, K. Tanaka, A. Fujimori, M. Okusawa, S. Wakimoto, K. Yamada, T. Kakeshita, H. Eisaki, and S. Uchida, *Phys. Rev. B* **75**, 140503(R) (2007); **79**, 140502(R) (2009).
- [43] G. Martinez and P. Horsch, *Phys. Rev. B* **44**, 317 (1991).
- [44] Z. Liu and E. Manousakis, *Phys. Rev. B* **45**, 2425 (1992).
- [45] R. Coldea, S. M. Hayden, G. Aeppli, T. G. Perring, C. D. Frost, T. E. Mason, S.-W. Cheong, and Z. Fisk, *Phys. Rev. Lett.* **86**, 5377 (2001).
- [46] A. A. Katanin and A. P. Kampf, *Phys. Rev. B* **66**, 100403(R) (2002).
- [47] M. Takahashi, *Phys. Rev. B* **40**, 2494 (1989); D. J. Yoshioka, *J. Phys. Soc. Jpn.* **58**, 3733 (1989).
- [48] V. Yu. Irkhin, A. A. Katanin, and M. I. Katsnelson, *Phys. Rev. B* **60**, 1082 (1999).
- [49] Y. Shimizu, K. Miyagawa, K. Kanoda, M. Maesato, and G. Saito, *Phys. Rev. Lett.* **91**, 107001 (2003).
- [50] Y. Kurosaki, Y. Shimizu, K. Miyagawa, K. Kanoda, and G. Saito, *Phys. Rev. Lett.* **95**, 177001 (2005).
- [51] A. Pustogow, M. Bories, A. Löhle, R. Rösslhuber, E. Zhukova, B. Gorshunov, S. Tomić, J. A. Schlueter, R. Hübner, T. Hiramatsu, Y. Yoshida, G. Saito, R. Kato, T.-H. Lee, V. Dobrosavljević, S. Fratini, and M. Dressel, *Nat. Mater.* **17**, 773 (2018).
- [52] T. Kobayashi, Q.-P. Ding, H. Taniguchi, K. Satoh, A. Kawamoto, and Y. Furukawa, *Phys. Rev. Res.* **2**, 042023(R) (2020).
- [53] P. G. J. van Dongen, *Phys. Rev. B* **50**, 14016 (1994).
- [54] G. Sangiovanni, A. Toschi, E. Koch, K. Held, M. Capone, C. Castellani, O. Gunnarsson, S.-K. Mo, J. W. Allen, H.-D. Kim, A. Sekiyama, A. Yamasaki, S. Suga, and P. Metcalf, *Phys. Rev. B* **73**, 205121 (2006).
- [55] We have verified that very close values are obtained using Padé analytical continuation of the self-energy with a fixed constant and $1/\nu$ asymptotics at large frequencies.